ACS Catalysis

pubs.acs.org/acscatalysis Research Article

# Inducing Microstrain in Electrodeposited Pt through Polymer Addition for Highly Active Oxygen Reduction Catalysis

Qi Hua, Xinyi Chen, Junfeng Chen, Nawal M. Alghoraibi, Yoon Lee, Toby J. Woods, Richard T. Haasch, Steven C. Zimmerman, and Andrew A. Gewirth*

Cite This: ACS Catal. 2024, 14, 7526–7535 Read Online

ACCESS | Metrics & More | Article Recommendations | Supporting Information

**ABSTRACT:** We investigate an approach to tune the d-band center and enhance the oxygen reduction reaction (ORR) activity of Pt material without relying on foreign metals or the process of alloying/dealloying. It is known that Pt exhibits suboptimal ORR catalytic activity due to its strong binding to oxygen, therefore requiring a downshift in the d-band center by approximately 0.2 eV to weaken the Pt-O binding energy and boost ORR kinetics. We found that the d-band center can be tuned by inducing microstrain in the Pt electrodeposit, simply achieved by introducing polymer into the electrodeposition bath. Pt electrodes (Pt-P1 and Pt-PLA) prepared with the addition of poly-*N*-(6-aminohexyl)acrylamide (P1) or poly-L-arginine (PLA) exhibit improved ORR activity compared to Pt electrodeposited without polymer addition (Pt-alone) in both acidic and basic environments, with the order of activity being Pt-P1 > Pt-PLA > Pt-alone. Pt-P1 exhibits a positive shift of $E_{1/2}$ by 90 mV vs Pt-alone in basic solution, comparable to other reported high-activity ORR catalysts. Scanning electron microscopy shows the presence of agglomerates with diameters between 5 and 20 $\mu$m and tip-splitting growth structure due to diffusion-limited aggregation on Pt-P1 and Pt-PLA. Characterization using X-ray photoemission spectroscopy and X-ray diffraction, combined with Rietveld refinement analysis reveal a trend of downshifted d-band center, increased microstrain, and slightly increased compressive strain as the ORR activity increased among the three catalysts. The presence of more defective sites on Pt-P1 and Pt-PLA is the cause of the increased microstrain, which further leads to the downshift of the Pt d-band center and enhancement of ORR activity.

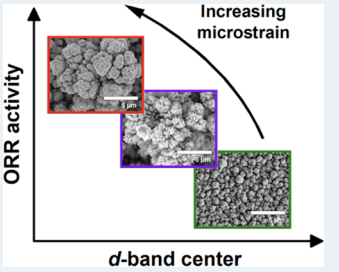


**KEYWORDS:** *oxygen reduction reaction, electrodeposition, d-band center shift, microstrain, surface defects, polymer*

## 1. INTRODUCTION

Fuel cells are next-generation energy-conversion devices to extract energy from chemical fuels.[1−3] Fuel cells feature fuel oxidation at the anode and typically oxygen reduction at the cathode. The sluggish cathode reaction, the oxygen reduction reaction (ORR), limits fuel cell energy efficiency. Despite decades of research, Pt and Pt-based alloys are still state-of-the-art ORR catalysts, particularly for acid electrolyte devices.[3−5]

Design strategies for better ORR catalysts aim to optimize catalyst adsorption strength of oxygenated species.[4] Numerous studies, however, suggest that Pt by itself is not the most optimized ORR catalyst since the adsorption energy of oxygenated species on elemental Pt is too large by ca. 0.1−0.2 eV.[6−12] The adsorption energy of oxygenated species is further directly correlated with the position of the d-band center of the Pt metal. The d-band center energy, in turn, depends on the electronic structure of the catalyst, which can be fine-tuned through the ligand (charge transfer) effect and strain (geometric) effect.[4,11−14] These effects are often found to work synergistically in changing the Pt electronic structure and d-band center.

Many recent studies directed toward maximizing ORR catalyst activity tune lattice strain by using different strategies such as metal alloying,[8,9,15,16] dealloying,[17−19] overlayer-support interactions,[10,20] and/or morphology control leading to nanostructures such as core−shell nanoparticles,[17] nanowires,[18,21] nanosheet,[22−24] nanocrystals,[25] and nanoframes,[26,27] among others. These strain-tuning strategies involve a foreign metal and are evidenced by changes in the Pt−Pt bond distance. Compressive strain (shortened Pt−Pt bond length) is usually concomitant with the downshift of the Pt d-band and consequently weakened adsorption of oxygenated intermediates.[4,11,13,28] For example, the compressive strain was induced in a dealloyed core−shell system where Cu was removed from a Pt−Cu alloy.[17] In another example, Pt deposited on chromium-doped titania support also exhibited enhanced ORR activity due to compressive strain in the deposit.[20]

Microstrain, a parameter of solid materials closely related to structural defects including atomic vacancies, grain boundaries, and multitwining, is another effective way to boost ORR activity.[19,25,29,30] For example, microstrain was correlated with

Received: February 27, 2024
Revised: April 19, 2024
Accepted: April 22, 2024
Published: April 30, 2024

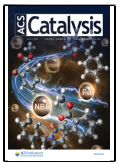







https://doi.org/10.1021/acscatal.4c01244
ACS Catal. 2024, 14, 7526−7535

ORR activity on PtNi/C nanostructures[25] and Pt-concave Ni-enriched (111) nanofacets.[29] In another example, increasing microstrain values on structurally disordered sponge PtNi/C nanocatalysts were correlated with increased ORR activity.[19] Defect-rich surfaces, such as stressed and undercoordinated crystalline-like surface rhombi on Pt−Ni nanowires were also correlated with high ORR activity.[18] Many other studies utilize defects to boost Pt-alloy ORR activity.[4,28,31] One feature of these works is the use of Pt alloys to create these defect sites.

Defect sites are also present on stepped single-crystal surfaces and correlated with improved ORR activity.[32−36] Studies on Pt single crystal show that stepped surfaces with different step atom densities exhibit enhanced activity compared to flat surfaces for reactions such as the ORR,[32−34,36] hydrogen evolution,[35] and hydrogen oxidation.[35] A recent density functional theory (DFT) study suggested that large surface strain is triggered by stress release present on Pt(111) step edges, which improves the site-specific catalytic activity by orders of magnitude compared to Pt(111) terrace sites.[37]

Electrodeposition is widely used to make electrocatalysts.[38−42] For example, we recently used amine-containing polymers to modify catalyst electrodeposits, resulting in an enhanced carbon dioxide reduction reaction and methanol oxidation reaction (MOR) activity.[43,44] In the case of the Cu electrodeposits, the polymer was found to be incorporated into the deposit,[43] but this was not the case for Pt.[44] We wondered whether the electrodeposition of Pt in the presence of different amine/guanidine-containing polymers might induce strain in the Pt lattice and thereby increase the ORR activity without recourse to a foreign metal.

In this paper, we evaluate the effect of polymer addition during Pt electrodeposition and show that different polymers yield different types of Pt electrodeposits. These electrodeposit structures are correlated with different degrees of microstrain, different d-band centers, and ultimately different ORR activity.

## 2. EXPERIMENTAL SECTION

**2.1. Catalyst Preparation.** Poly-*N*-(6-aminohexyl)-acrylamide (P1) was synthesized as described in the literature.[43] Poly-L-arginine hydrochloride or poly(L-Arg), simplified as "PLA" in this study, was obtained from Sigma-Aldrich and used without further purification. The structures of P1 and PLA are shown in Figures S1 and S2. Except where specified, other chemicals were obtained from Sigma-Aldrich and used without further purification.

The Pt-alone catalysts were electrodeposited from a solution containing 3 mM $H_2PtCl_6{\cdot}6H_2O$ and 0.1 M $NaClO_4$ using a modification of a literature procedure.[45] The Pt-PLA catalysts were electrodeposited using the same solution as the Pt-alone catalyst but with the addition of 1.6 $\mu$g/mL PLA. Galvanostatic electrodeposition was performed on the working electrode at a constant current density of −12 mA/cm$^2$ for 450 and 900 s for Pt-alone and Pt-PLA, respectively, at a rotation rate of 1600 rpm. The Pt-P1 catalysts were electrodeposited from a solution containing 3 mM $H_2PtCl_6{\cdot}6H_2O$ and 120 $\mu$g/mL (6 $\mu$M) P1 without the addition of $NaClO_4$ supporting electrolyte salt. The supporting electrolyte was found to inhibit the effect of P1 addition to the plating bath. Galvanostatic electrodeposition was performed on the working electrode at a constant current density of −24 mA/cm$^2$ for 900 s.

Electrodeposition was performed using either a polycrystalline Pt disk ($A$ = 0.201 cm$^2$) or a polycrystalline Au disk ($A$ = 0.199 cm$^2$) as the working electrode. The electrode was rotated at 1600 rpm to obtain an evenly deposited film. The Pt or Au disk was polished sequentially with 9, 3, and 1 $\mu$m diamond polish (Buehler) and rinsed with Milli-Q water before electrodeposition. A Pt wire was used as the counter-electrode and a leakless Ag/AgCl (eDAQ) electrode was used as the reference electrode. The electrochemically active surface area (ECSA) of the catalysts was determined from charges associated with underpotentially deposited H ($H_{upd}$). The desorption peaks of $H_{upd}$ from recorded CVs were used to calculate the ECSAs, assuming a charge density of 210 $\mu$C/cm$^2$ for one monolayer of hydrogen coverage on Pt.[46] A typical deposition passed 10.8 C/cm$^2$ of charge with a 0.2 cm$^2$ working electrode removing ca. 4% of the available Pt in solution. Based on gravimetric measurements, the catalyst loading was around 0.3−0.6 mg yielding a Pt loading of ca. 2.5 mg/cm$^2$ and the estimated Faradaic efficiency for Pt deposition was ca. 40%. We note that the Pt loading achieved by our electrodeposition method is about 300-fold higher than that found on carbon-supported highly dispersed Pt materials (e.g., 7.5 $\mu$g/cm$^2$).[22]

**2.2. Electrochemical Experiments.** Electrochemical measurements were performed in a 3-compartment electrochemical cell. The working, counter, and reference electrodes were the modified Pt or Au disk, a carbon rod, and a "leakless" Ag/AgCl (3 M KCl) reference electrode (eDAQ), respectively. Aqueous electrolyte solutions were prepared using Milli-Q purified water (>18 MΩ cm), $HClO_4$ (ultrapure, J.T. Baker), or KOH (Fisher Chemical) for acidic and alkaline environments, respectively. For the kinetic isotope study, deutero aqueous solutions were prepared using $D_2O$ and KOD. Solutions were sparged with $O_2$ or Ar before each measurement for 30 min.

Cyclic voltammetry (CV) was measured using a rotating disk electrode (RDE) on a 760D Electrochemical Workstation (CH Instruments, Austin, TX) and an MSRX rotator (Pine Instruments, Durham, NC) between relevant voltages, with a 5 mV/s scan rate in Ar-saturated electrolyte solutions at a rotation rate of 1600 rpm. All potentials were converted to the reversible hydrogen electrode (RHE) scale by measuring the open-circuit potential of a flame-annealed Pt wire electrode in $H_2$ gas-saturated electrolyte before each measurement and are reported vs RHE. Staircase voltammetry was conducted between relevant voltages by using a 0.01 V step increment, 0.0167 s sampling width, and 30 s step period in $O_2$-saturated electrolyte solutions. The ORR activity was estimated using the kinetic current $i_k$ at 0.95 V vs RHE calculated using the Koutecký−Levich equation: $\frac{1}{i} = \frac{1}{i_k} + \frac{1}{i_{lim}}$, where $i$ and $i_{lim}$ are the measured current and diffusion-limited current, respectively. The corresponding kinetic current density $j_k$ at a given potential was obtained by normalizing the $i_k$ using the geometric area of the electrode (0.201 cm$^2$). Accelerated durability tests were conducted by cycling between 0.6 and 1.0 V versus RHE at 50 mV/s for 2000 cycles. Values reported reflect the results of at least three independent measurements.

**2.3. Physical Characterization.** Scanning electron microscope (SEM) images were obtained with FEI Helios 600i Dual Beam SEM/FIB. X-ray photoelectron spectroscopy (XPS) was performed using a Kratos AXIS SUPRA$^+$ spectrometer with a monochromatic Al K$\alpha$ (1486.69 eV) X-ray source. All binding energies were referenced to the Fermi level (0.00 eV) of projected d-band density-of-states (DOS) of Pt. The Shirley-


https://doi.org/10.1021/acscatal.4c01244
ACS Catal. 2024, 14, 7526−7535

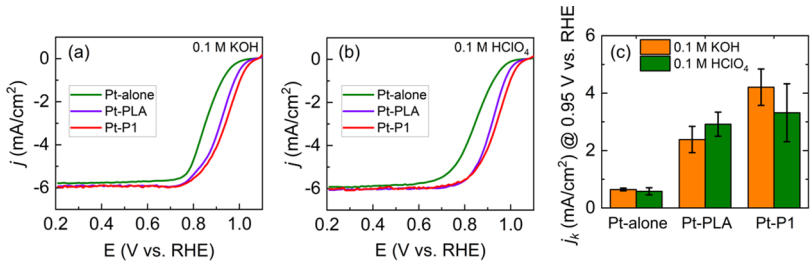


**Figure 1.** Staircase voltammograms (SCVs) of Pt-alone, Pt-PLA, and Pt-P1 in $O_2$-saturated (a) 0.1 M KOH and (b) 0.1 M $HClO_4$ using an RDE at 1600 rpm; (c) comparison of kinetic current density ($j_k$) for the Pt-alone, Pt-PLA and Pt-P1 catalysts at 0.95 V vs RHE measured in both 0.1 M KOH (orange) and 0.1 M $HClO_4$ (green) solution.

background subtracted XPS valence band spectra (binding energy from −2 to 16 eV) were used to calculate the d-band centers of Pt. The d-band center was calculated as the weighted average binding energy.[47,48] The negative sign indicates that the d-band center is below the Fermi level. XRD patterns were collected using a Bruker D8 Advance X-ray diffractometer equipped with a 2 mm collimator and a Cu K$\alpha$ source. XRD was performed on Pt(poly) and Pt deposited onto an Au(poly) substrate to clearly distinguish the Pt electrodeposit from the substrate. The electrochemical activity of the Pt electrodeposit on Au was found to be identical to that of the Pt electrodeposited on Pt.

**2.4. Rietveld Refinements.** Rietveld refinements were carried out using TOPAS Version 4.2 for 2$\theta$ between 20° and 90°. The instrumental broadening was determined by the refinement of a $LaB_6$ standard sample. Since the XRD spectra were collected on Pt samples that were electrodeposited on a polycrystalline gold disk, two phases were used for the refinement: the Pt phase was refined against the known structure of metallic Pt (PDF#97-005-2250); because of severe preferred orientation and a large sample offset, refining the peaks from the gold substrate was more successful using an *hkl* phase in space group $Fm\bar{3}m$ with an initial lattice parameter consistent with metallic gold. Refinements considered the zero error, sample displacement, instrumental broadening, lattice constant, and size- and strain-induced Gaussian-/Lorentzian peak broadening. Additional possible components to the fit, such as interstitial oxygen, were not considered.

## 3. RESULTS

**3.1. Electrochemical Experiments.** *3.1.1. ORR Activity.* Figure 1a shows the ORR catalytic activity obtained from an RDE electrodeposited with Pt-alone (green trace), Pt-PLA (purple trace), and Pt-P1 (red trace), respectively, in 0.1 M KOH. All three catalysts exhibit the typical sigmoidal CV curve shape with similar diffusion-limited current at around 6 mA/cm$^2$, while the onset and half-wave potentials ($E_{1/2}$) differ among the three catalysts. The Pt-alone catalyst shows an $E_{1/2}$ at 0.85 ± 0.01 V, which is close to the $E_{1/2}$ value of the commercial Pt/C.[49,50] Both Pt-PLA and Pt-P1 exhibit an anodic shift of $E_{1/2}$ which indicates enhanced ORR activity compared to Pt-alone or Pt/C. Specifically, Pt-PLA shows an $E_{1/2}$ at 0.91 ± 0.01 V with a shift of 60 mV relative to Pt-alone. Pt-P1 shows an $E_{1/2}$ at 0.94 ± 0.01 V with a shift of 90 mV relative to Pt-alone. This $E_{1/2}$ achieved on Pt-P1 is comparable with other reports of high-performance ORR catalysts in alkaline media.[18,22]

The ORR activity for the three catalysts was also examined in 0.1 M $HClO_4$ as shown in Figure 1b. The SCVs of all three catalysts in acid exhibit $E_{1/2}$ values (Table 1) similar to those found in the basic environment. Notably, in acidic conditions,

**Table 1. ORR Performance of Pt-alone, Pt-PLA, and Pt-P1 Catalysts in 0.1 M KOH and 0.1 M $HClO_4$[a]**

| electrolyte | electrode | $E_{1/2}$ (V vs RHE) | $n$ at 0.4 V vs RHE | Tafel slope (mV/dec) |
|---|---|---|---|---|
| 0.1 M KOH | Pt-alone | 0.85 ± 0.01 | 3.91 ± 0.04 | 57 ± 7; 99 ± 5 |
| | Pt-PLA | 0.91 ± 0.01 | 4.01 ± 0.03 | 42 ± 6; 88 ± 12 |
| | Pt-P1 | 0.94 ± 0.01 | 4.05 ± 0.07 | 42 ± 2; 85 ± 7 |
| 0.1 M $HClO_4$ | Pt-alone | 0.85 ± 0.01 | 3.96 ± 0.13 | 61 ± 5; 109 ± 13 |
| | Pt-PLA | 0.92 ± 0.01 | 4.11 ± 0.04 | 50 ± 5; 84 ± 3 |
| | Pt-P1 | 0.93 ± 0.01 | 4.02 ± 0.08 | 37 ± 4; 77 ± 9 |

[a]The errors represent the standard deviations of at least three independent measurements.

the $E_{1/2}$ of the Pt-PLA and Pt-P1 catalysts still demonstrate a positive shift of 70 and 80 mV, respectively, when compared to Pt-alone. Figure 1c illustrates the measured kinetic current density ($j_k$) at 0.95 V for three catalysts in both alkaline (orange columns) and acidic (green columns) solutions. The 0.95 V potential was chosen to produce a reliable kinetic current density and eliminate $O_2$-diffusion limits.[22] Pt-alone exhibits a $j_k$ = 0.64 mA/cm$^2$ in both basic and acidic solutions. For Pt-PLA, $j_k$ increases by a factor of 4 and 5 in basic and acidic solutions, respectively, relative to Pt-alone. Likewise, Pt-P1 exhibits an increased $j_k$ relative to Pt-alone by a factor of 7 and 5.5 in basic and acidic solutions, respectively. Both the anodic $E_{1/2}$ shift and increased $j_k$ indicate that the polymer-incorporated Pt-PLA and Pt-P1 exhibit enhanced ORR kinetics relative to the Pt-alone catalyst. The performance of Pt-P1 is slightly superior to Pt-PLA.

The number of electrons transferred for Pt-alone, Pt-PLA, and Pt-P1 was determined from Levich plots (Table 1, Figure S3) to be 3.91, 4.01, and 4.05 in basic solution and 3.96, 4.11, and 4.02 in acidic solution, which suggests a 4-electron pathway from $O_2$ to $OH^-$ or $H_2O$. The reason for observing n larger than 4 might come from the less than perfect laminar flow caused by the rough electrode surface.[51,52]

*3.1.2. Characteristic CV.* Figure 2 shows the voltammetry curves obtained from a solution containing 0.1 M $HClO_4$ for Pt-alone, Pt-PLA, and Pt-P1. The voltammetry curves of all three catalysts show the H-underpotential deposition (H-UPD) waves between 0.0 and 0.4 V, followed by waves associated with Pt-oxide formation and reduction between 0.4 and 1.2 V. The ECSA obtained from the H-UPD region for the Pt-alone sample was 51 ± 9 cm$^2$, while Pt-PLA and Pt-P1 have much larger ECSA of 132 ± 24 and 180 ± 27 cm$^2$,


https://doi.org/10.1021/acscatal.4c01244
ACS Catal. 2024, 14, 7526−7535

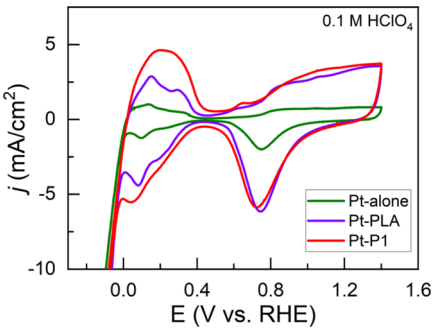


**Figure 2.** Cyclic voltammograms (CVs) obtained from Pt-alone, Pt-PLA, and Pt-P1 in Ar-saturated 0.1 M $HClO_4$ at a scan rate of 5 mV/s using an RDE at 1600 rpm.

respectively. The H-UPD curve is also known to be structure-sensitive.[53−55] In the H-UPD region, the voltammetry curves associated with Pt-PLA are similar to that seen from Pt-alone, with two pairs of symmetrical peaks that are usually associated with the presence of Pt(110) and Pt(100) facets.[56,57] However, the Pt-P1 CV shows a broad hump in this region without any well-resolved peaks. The origin of this broad peak on Pt-P1 could be due to the higher degree of structural disorder and/or more surface defects created during the Pt-P1 deposition process (vide infra).

An interesting feature of the Pt-P1 CV is the ratio between the integrated charge associated with the oxide reduction (0.5−1.2 V) and hydrogen desorption (0−0.4 V) ($Q_O/Q_H$). Both Pt-PLA and Pt-alone show $Q_O/Q_H \approx 2$, while Pt-P1 has a $Q_O/Q_H = 1.3$. Pt-poly is also reported to exhibit a $Q_O/Q_H \approx 2$ after a first cycle CV with an upper potential limit of 1.4 V vs RHE.[58−60] Pt oxidation occurs in two steps. First, a monolayer of Pt−OH forms between 0.8 and 1.1 V, followed by further oxidation to an oxide PtO (one O atom per Pt atom, not a stoichiometric compound) in a so-called place-exchange over the broad region from 1.1 to 1.4 V.[60] The lower value of $Q_O/Q_H$ for Pt-P1 following cycling to 1.4 V indicates that further oxidation of the Pt−OH layer on this surface is inhibited. The oxide reduction peaks for Pt-alone, Pt-PLA, and Pt-P1 are at 0.75 ± 0.01, 0.74 ± 0.01, and 0.72 ± 0.02 V, respectively. No significant difference was found in terms of the oxide reduction peak positions for the three catalysts.

*3.1.3. Tafel Plots.* Figure 3 shows the Tafel plots for Pt-alone, Pt-PLA, and Pt-P1 catalysts measured in both 0.1 M KOH (Figure 3a) and 0.1 M $HClO_4$ (Figure 3b) solutions. The measured Tafel slopes with errors are tabulated in Table 1. Previous reports show that the ORR Tafel plot usually depicts two slopes: a value of 60 mV/dec at lower overpotentials and a value of 120 mV/dec at higher overpotentials, where the 120 mV/dec Tafel slope is interpreted as suggesting that the first electron transfer is rate-limiting.[61,62] The two-step Tafel slope has been associated with two different mechanisms at different overpotentials[61] and/or potential-dependent oxygen intermediate coverages on the Pt surface.[63−65] Pt-alone exhibits the typical two-step Tafel slope changing from 61 ± 5 mV/dec (at lower overpotential) to 109 ± 13 mV/dec (at higher overpotential) in acid and from 57 ± 7 to 99 ± 5 mV/dec in base. These values are close to the Tafel slopes found for Pt/C in both acidic and alkaline conditions.[51] Pt-PLA and Pt-P1 also show two-step Tafel slopes but with smaller slopes in both low and high overpotential regions. Specifically, Pt-PLA has Tafel slopes of 42 ± 6 and 88 ± 12 mV/dec in base and 50 ± 5 and 84 ± 3 mV/dec in acid. Pt-P1 has Tafel slopes of 42 ± 2 and 85 ± 7 mV/dec in base and 37 ± 4 and 77 ± 9 mV/dec in acid. The smaller Tafel slopes found on Pt-PLA and Pt-P1 are consistent with the increased kinetics of the ORR found above.

In order to evaluate whether the presence of the polymer in the electrodeposition bath might change the ORR mechanism, we measured the kinetic isotope effect (KIE) for the ORR on Pt-alone and Pt-P1 (Figure S4). The KIE was 1.07 ± 0.32 for Pt-alone and 0.92 ± 0.37 for Pt-P1. These observed KIEs around unity agree well the unity KIE for Pt ORR found previously.[66,67] This unity KIE indicates that the ORR rate-determining step (RDS) is a proton-independent electron transfer step.[67,68] Thus, the presence of the polymer in the Pt electrodeposition bath does not change the ORR mechanism.

The electrochemical durability of the three catalysts in alkaline electrolytes was assessed by accelerated stability test (AST) between 0.6 and 1.0 V at 50 mV/s in $O_2$-saturated 0.1 M KOH solutions for 2000 potential cycles. Figure S5 shows the ORR staircase voltammograms obtained before and after the AST test for Pt-alone, Pt-PLA, and Pt-P1. The ORR curves for all three catalysts exhibit a negative shift of $E_{1/2}$ by 30−40 mV after cycling, consistent with prior reports.[69−72] Pt-P1 and Pt-PLA exhibit comparable durability as Pt-alone.

**3.2. Physical Characterization.** *3.2.1. SEM.* Figure 4 shows the SEM images obtained for Pt-alone, Pt-PLA, and Pt-P1. The first row shows plan-view SEM images of the top of the electrodes, while the second row shows cross-sectional SEM images observed at a 52° angle after creating a cross

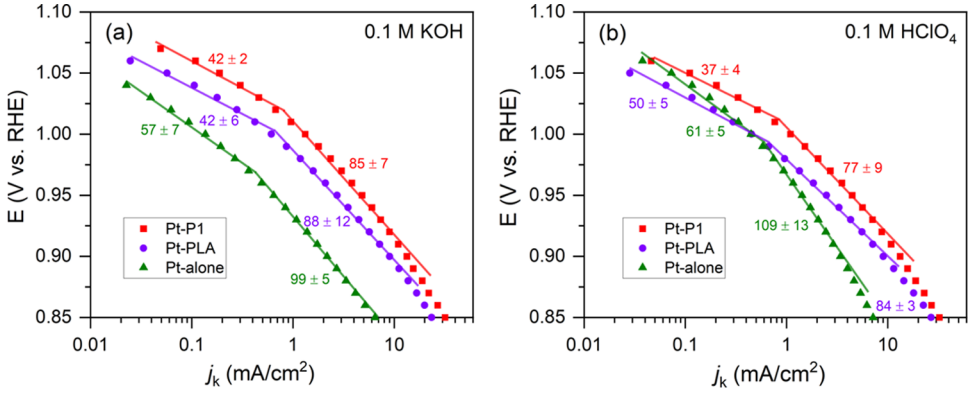


**Figure 3.** Tafel plot ($E$ vs $j_k$) of Pt-alone, Pt-PLA, and Pt-P1 catalysts in $O_2$-saturated (a) 0.1 M KOH and (b) 0.1 M $HClO_4$. The measured Tafel slopes (unit: mV/dec) with errors derived from multiple measurements are shown next to the lines.



https://doi.org/10.1021/acscatal.4c01244
ACS Catal. 2024, 14, 7526−7535

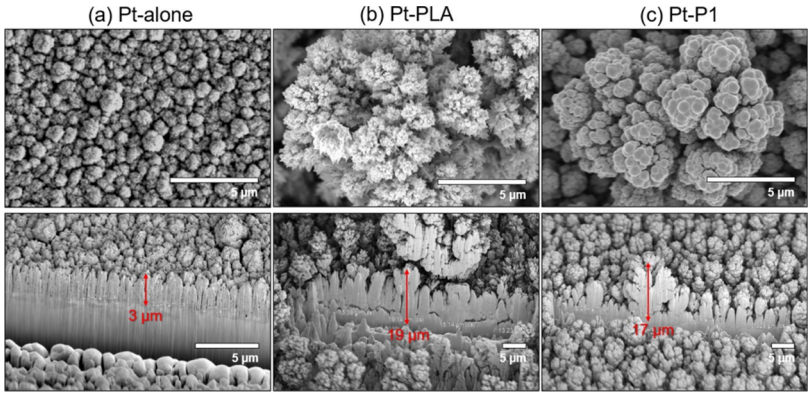


**Figure 4.** Plan-view (first row) and cross-sectional (second row) SEM images of (a) Pt-alone, (b) Pt-PLA, and (c) Pt-P1. The corresponding scale bar is shown at the bottom right of each image. The numbers below each red arrow indicate the thickness of the corresponding deposited catalyst layer.

section using ion milling on the three electrode surfaces. The horizontal particle/agglomerate size and the deposit layer thickness can be obtained from the plan-view and cross-sectional SEM images, respectively. All SEM images show the presence of deposits that have nucleated on the surface and grown. The Pt-alone deposit shows a particle size of ca. 1 $\mu$m with a more uniform layer thickness of ca. 3 $\mu$m. Pt-PLA and Pt-P1 deposits show the presence of additional complexity in the deposit likely associated with the higher surface area found above. Pt-PLA exhibits sharp-texture agglomerates with diameters from 5 to 20 $\mu$m, and a layer thickness from 10 to 30 $\mu$m. Pt-P1 exhibits agglomerates with a smoother texture with diameters from 5 to 20 $\mu$m and a layer thickness from 8 to 20 $\mu$m.

Different growth patterns during electrodeposition reflect differing rates of deposition and the presence of inhibitors.[73] Columnar growth occurs because of the natural roughing of the deposit following the initial nucleation and growth phase. This roughening leads to asperities which continue to grow into columns under moderately high deposition rates.[74] The cross-sectional image of Pt-alone shows a columnar structure. The presence of tip splitting found with both Pt-PLA and Pt-P1 indicates that diffusive processes leading to columnar growth are further diminished and growth via diffusion-limited aggregation occurs. The amine or guanidine functional groups from the polymer additives complex with Pt(IV) in the plating bath and suppress the diffusion of Pt cation during the crystal growth.[75,76] Pt-P1 was grown with a current density a factor of 2 greater than that for Pt-PLA. This lower current density coupled with weaker complexation of PLA with Pt(IV) (vide infra) may be the origin of the somewhat diminished tip splitting seen in the cross-sectional SEM for Pt-PLA. Other combinations of current density, polymer concentration, supporting electrolyte, and deposition time would undoubtedly yield different morphologies.

*3.2.2. XPS.* We conducted the XPS analysis to characterize the electronic structure of the catalyst samples. XPS obtained in the N 1s region showed a weak signal that was lower in the Pt-P1 or Pt-PLA samples relative to either Pt(poly) or Pt-alone (Figure S6(a)). Additionally, XPS obtained in the Pt 4f region from the different samples were also independent of polymer presence in the plating bath (Figure S6(b)). Thus, polymer incorporation into the Pt lattice is likely low.

Figure 5 shows the valence band photoemission spectra of the as-prepared Pt-alone, Pt-PLA, and Pt-P1 catalysts along

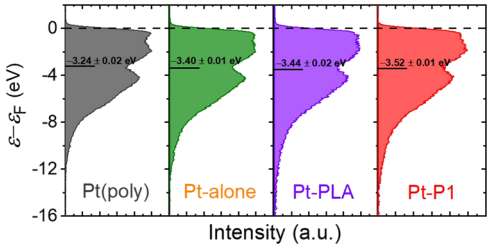


**Figure 5.** XPS profiles in the valence band region for Pt(poly), Pt-alone, Pt-PLA, and Pt-P1 with Shirley-background subtraction. The black horizontal dashed line indicates the Fermi level at 0.00 eV. The short black lines represent the d-band centers of each sample relative to the Fermi level, with their corresponding errors.

with polycrystalline Pt as a reference. The Shirley-background subtracted XPS valence band profile between 2 and −16 eV (relative to Fermi level) was used to determine the location of the d-band center.[77] The d-band center for Pt(poly) is found at −3.24 eV, which is within the (large) range of other experimental reports of the Pt d-band center (ranging from −4.0[47] to −3.45 eV[78] to −2.5 eV[77]). This large range in the experimentally measured d-band center is said to be associated with several factors such as the choice of photon energy, treatment of background, selection of the integration limit, the adsorption of residual gas, and sample treatment.[48]

In our measurements, samples were processed identically and provided a robust relative shift of d-band centers between the different samples. Figure 5 shows that the d-band center gradually downshifts from left to right with the trend: Pt(poly) > Pt-alone > Pt-PLA > Pt-P1. Pt-P1 which exhibits the highest activity (Figure 1) among the three electrodeposited samples also exhibits the greatest d-band downshift of 0.28 eV relative to Pt(poly) while Pt-alone has a shift of only 0.16 eV.

Figure 6 reports the correlation between the d-band center and the corresponding catalytic activity (expressed as $E_{1/2}$ measured in an alkaline environment) of the catalysts. The plot shows a roughly linear relationship between the d-band center and the catalyst ORR activity, where the higher ORR activity was found on the catalyst with a lower d-band center. A similar correlation is found by plotting $j_k$ versus the d-band center in both alkaline and acidic media (Figure S7).

*3.2.3. XRD and Rietveld Refinement.* Figure 7 shows the X-ray diffraction pattern collected from Pt-alone, Pt-PLA, and Pt-P1 electrodeposited on Au disks. We used the Au substrate


https://doi.org/10.1021/acscatal.4c01244
ACS Catal. 2024, 14, 7526−7535

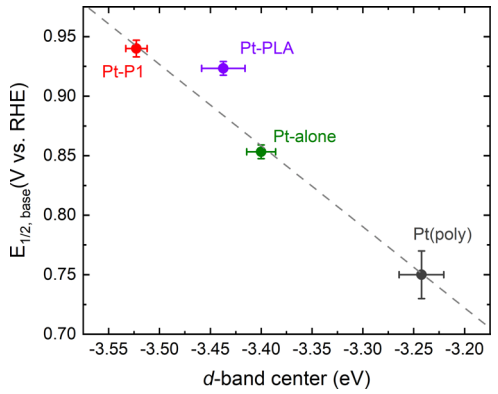


**Figure 6.** Relationships between the ORR half-wave potential in base ($E_{1/2,\ base}$) and the d-band center location for samples inspected in this study.

instead of Pt to more easily deconvolute the diffraction from the electrodeposited Pt film with that from the substrate. We also collected XRD from a polycrystalline Pt disk for reference. Figure 7a shows that Pt(poly) exhibits the typical peak positions associated with the face-centered cubic (fcc) structure of Pt metal. Larger peak intensity from the Pt (200) reflection compared to Pt (111) is evidence of preferential orientation toward Pt (200) on this Pt(poly) disk. The patterns obtained on Pt-alone, Pt-PLA, and Pt-P1 all exhibit peaks from both Pt fcc and Au fcc phases. The peaks associated with Pt and Au phases are well-resolved for almost the whole pattern ranging from 30 to 90° (except for the overlapping Pt (311) and Au (222) peaks). Therefore, Rietveld refinement can be leveraged to extract details of structural changes in the modified Pt-film. The best refinement results were obtained using a Pt phase and an *hkl* phase. Detailed values of the structural parameters are given in Table S1, and the refinement deconvolutions are presented in Figure S8.

Figure 7b–d shows the lattice parameter *a*, the microstrain $e_0$, and the mean crystallite size obtained from Rietveld refinement for all four samples. The change of the lattice parameter *a* indicates global lattice expansion/contraction relative to a reference, which is referred to as "global strain" or "macrostrain".[19] Figure 7b shows a trend of increasing lattice contraction from Pt(poly) to Pt-P1 as evidenced by the decreased value of *a*. This lattice contraction can also be observed as a slight peak shift to higher angles of the (111) peak from Pt(poly) to Pt-P1 in Figure 7a. The lattice contraction found here (0.3% for Pt-P1 relative to Pt(poly)) is an order of magnitude smaller than that found for the dealloyed Pt-M materials (ca. 2–4%)[17,19] which also exhibit enhanced ORR activity relative to Pt(poly). The diminished compressive strain found here may reflect an average strain where a highly strained surface is compensated by less strain in the bulk.

Microstrain, also referred to as "local lattice strain", is a measure of the local deviation of the atoms from their ideal positions in the lattice structure, a deviation that contributes to XRD peak broadening but not peak shifting.[25] Microstrain has been used to evaluate structural disorder induced by structural defects such as stacking faults, twins, grain boundaries, and dislocation arrays.[19,25,29,30] Figure 7c shows the raw microstrain obtained from Rietveld refinement without any further processing. Pt-alone and Pt-PLA both exhibit much larger microstrain values than that observed on nearly nonstrained Pt(poly). Pt-PLA also exhibits slightly increased microstrain compared to Pt-alone. Interestingly, Pt-P1 shows the highest degree of microstrain, with a value that is about twice as large as Pt-alone. This change in microstrain can be visualized in the moderately broad peaks found for Pt-alone and Pt-PLA and the broadest peaks found for Pt-P1 (e.g., Pt (220) peak) in Figure 7a. The microstrain values found here are close to those reported for PtNi nanoparticles (0.4–0.8) using the same refinement software (TOPAS 4.2).[29]

Both microstrain and diminished crystallite size can generate peak broadening in XRD patterns. Figure 7d shows the refined mean crystallite sizes (structural coherence length) obtained for Pt-alone, Pt-PLA, and Pt-P1. The crystallite sizes found are

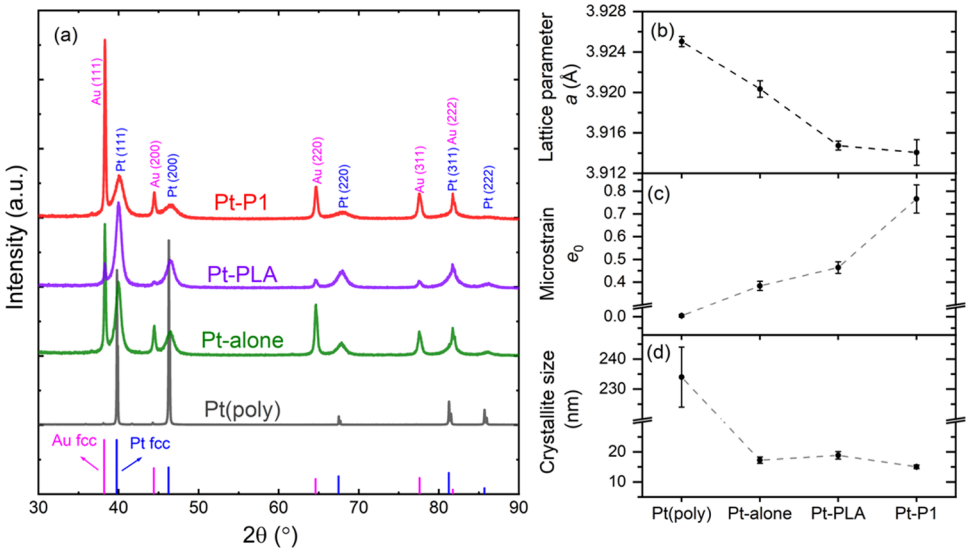


**Figure 7.** X-ray diffraction pattern and analysis. (a) Measured XRD patterns of Pt(poly), Pt-alone, Pt-PLA, and Pt-P1 samples prepared on a polycrystalline Au disk. The blue and pink bars indicate pure metals Pt fcc (PDF #97-005-2250) and Au fcc (PDF #00-066-0091). (b–d) structural parameters obtained from Rietveld refinement: (b) lattice parameter *a*, (c) microstrain $e_0$, and (d) crystallite size. Gray dashed lines are a guide to the eye.



https://doi.org/10.1021/acscatal.4c01244
ACS Catal. 2024, 14, 7526–7535

all about the same (ca. 17 nm), much smaller than the crystallite size of pure Pt(poly) (234 nm). The similarity in crystallite size for the three electrodeposited Pt samples implies the different degrees of peak broadening among Pt-alone, Pt-PLA, and Pt-P1 in Figure 7a are mainly governed by differences in microstrain rather than in crystallite size.

## 4. DISCUSSION

The electrochemical results show that the electrodeposition of Pt in the presence of different N-containing polymers can yield materials exhibiting high ORR activity. Pt-P1 can achieve an $E_{1/2}$ = 0.95 V in an alkaline solution and $E_{1/2}$ = 0.94 V in an acidic solution, consistent with the best reports to date.[18,22] Pt-PLA also exhibits improvement in ORR performance compared to Pt-alone with an $E_{1/2}$ of 0.92 V in alkaline solution and $E_{1/2}$ = 0.93 V in acidic solution. We note, however, that the mass or specific activity of the catalysts reported here is somewhat lower than other reports due to the large Pt loading onto the electrode. The improvement of ORR kinetics is also reflected in the lower Tafel slopes for Pt-P1 and Pt-PLA relative to Pt alone.

The improvement in ORR activity found for Pt-P1 and Pt-PLA is correlated with both the presence of a decreased d-band center and a corresponding increase in microstrain in the deposits. The morphology of the Pt-P1 and Pt-PLA materials is consistent with growth via diffusion-limited aggregation, which is likely the origin of the increased microstrain and d-band center decrease.

Numerous experimental[9,10,15,17,47] and computational studies[8,12] suggested that Pt binds oxygen too strongly, resulting in a relatively high $O_2$ dissociation energy barrier. It was predicted that a downshift of the d-band center by ca. 0.2 eV relative to the Pt(111) surface is optimal to weaken the Pt-O binding energy and enhance the ORR kinetics.[4,10] A downshift of 0.28 ± 0.02 eV is found in the Pt-P1 catalyst, and a lesser downshift of 0.20 ± 0.03 eV is found in the Pt-PLA catalyst.

The origin of the lower d-band center in the Pt-P1 material is likely due to the presence of microstrain. The correlation of increased activity with increased microstrain has been observed previously in porous hollow or sponge-like PtNi/C nanocrystals.[19,25,29] The high microstrain values reported in these systems reflect the highly defective surfaces produced by abundant grain boundaries. The origin of the improved ORR activity on the defective PtNi/C nanostructure was suggested to be due to a wide distribution of catalyst site configurations, where the sites with close-to-optimal Pt-O binding energy likely contribute the most to the overall ORR activity.[19] Indeed, recent DFT calculations suggest that substantial compressive strain is present at step-type defects on Pt(111), which is driven by the stress release on both sides of step edges.[37] The magnitude of this atomic site-specific strain is more pronounced at a narrower terrace width, e.g., −4.7% strain is induced by the Pt(221) terrace edge. This work predicted that the site-specific compressive strain lowers the d-band center, weakens the adsorption strength of ORR intermediates, and enhances the ORR activity by orders of magnitude on these step-type defects,[37] effects which are exactly observed here.

Other computational work suggests the presence of atomic stress on defective and undercoordinated sites on jagged Pt nanowires[18] and fully dealloyed $Pt_3Ni_7$ nanoparticles,[79] both of which exhibit high ORR activity. This calculated atomic stress is at least an order of magnitude higher than the values found on more regular structures such as Pt nanowires with a relatively smooth surface[18] or truncated-octahedral Pt particles.[79] The high atomic stress mentioned in these papers was suggested to be correlated with the experimentally measured surface strain and enhanced ORR catalytic behavior.[18,79]

We suggest here that the higher degree of microstrain found for Pt-P1 indicates the presence of more defective sites. These defective sites, mostly present on the surface of Pt-P1 deposits, can release atomic stress and consequently generate local compressive strain. The compressive strain further leads to a downshift in the d-band center of Pt in Pt-P1.[13] Pt-PLA also exhibits increased microstrain relative to Pt-alone but less than Pt-P1. This intermediate increased microstrain also results in a decreased d-band center, but the shift is less than that found for Pt-P1. Thus, the ORR activity for Pt-PLA is not as high as that for Pt-P1.

The overall origin of high ORR activity is then related to defects formed during the electrodeposition of the Pt electrode in the presence of different polymers even though the polymers were not found to be incorporated into the Pt deposits. The origin of the different degrees of defect incorporation must relate to the differing electrodeposition parameters, including different degrees of polymer association with $[PtCl_6]^{2-}$ in the electrodeposition bath. The protonated primary amine group ($pK_a \sim 10.5$) is less basic than the protonated guanidine group ($pK_a \sim 12.5$),[80] the amine groups present on P1 therefore have stronger coordination to Pt compared to the guanidinium group on PLA. Indeed, the equilibrium constant for an anion-exchange reaction of $[PtCl_6]^{2-}$ with different amines ranges from $10^3$ to $10^6$.[75,76,81]

Several features from the characteristic CV of Pt-P1 support the results of changed Pt electronic structure (downshifted d-band center) and increased surface defectivity mentioned above (Supporting Information, S9). First, the lower $Q_O/Q_H$ indicates a lower oxide coverage for Pt-P1 relative to Pt-alone. The origin of this diminished oxide coverage is likely the decreased d-band center in Pt-P1, which leads to weakened adsorption of oxygen-containing intermediates on the Pt-P1 surface. Second, the broad peak found in the H-UPD region (0−0.4 V) on Pt-P1 is further evidence of the presence of a defective surface with structures (terraces, steps, kinks) exhibiting numerous facets. We note, however, that both the lower oxide coverage and the broad H-UPD feature were not clearly seen on Pt-PLA, possibly due to the intermediate degree of lowered d-band center and microstrain.

## 5. CONCLUSIONS

This study shows that the addition of amine or guanidine-containing polymers during Pt electrodeposition changes the electrodeposit morphology by accessing diffusion-limited aggregation growth. The higher ORR activity of these electrodeposited catalysts is correlated with the downshift of the d-band center and higher surface microstrain originating from structural defects in the deposits. The high defectivity of the catalyst surface likely produces surface atomic stress, leading to local lattice compression and downshift of the Pt d-band center. The lower d-band center weakens the adsorption strength of oxygenated species, which in turn boosts the ORR kinetics. The magnitude of d-band shift is then directly correlated with surface defectivity. In turn, the degree of defects is regulated by electrodeposition bath parameters, among which is changing the degree of coordination between


https://doi.org/10.1021/acscatal.4c01244
ACS Catal. 2024, 14, 7526−7535

the polymer additive and Pt(IV) in the electrodeposition bath. While the relatively high Pt loading reported here makes direct application of the electrodeposition protocol toward a device unlikely, the protocol does provide an additional procedure through which Pt activity can be tuned.

## ■ ASSOCIATED CONTENT

### Supporting Information

The Supporting Information is available free of charge at https://pubs.acs.org/doi/10.1021/acscatal.4c01244.

Structure of P1 and PLA; Koutecký−Levich plots; kinetic isotope effect (KIE); durability test; N 1s and Pt 4f XPS spectra; correlation between d-band and ORR activity; TOPAS Rietveld refinement results; and voltammetry discussion (PDF)

## ■ AUTHOR INFORMATION


### Corresponding Author

**Andrew A. Gewirth** − *Department of Chemistry, University of Illinois at Urbana—Champaign, Urbana, Illinois 61801, United States;* orcid.org/0000-0003-4400-9907; Phone: 217-333-8329; Email: agewirth@illinois.edu; Fax: 217-244-3186

### Authors

**Qi Hua** − *Department of Chemistry, University of Illinois at Urbana—Champaign, Urbana, Illinois 61801, United States;* orcid.org/0000-0002-7857-6638

**Xinyi Chen** − *Department of Chemistry, University of Illinois at Urbana—Champaign, Urbana, Illinois 61801, United States;* orcid.org/0000-0002-6990-5233

**Junfeng Chen** − *Department of Chemistry, University of Illinois at Urbana—Champaign, Urbana, Illinois 61801, United States;* orcid.org/0000-0002-7100-0839

**Nawal M. Alghoraibi** − *Department of Chemistry, University of Illinois at Urbana—Champaign, Urbana, Illinois 61801, United States*

**Yoon Lee** − *Department of Chemistry, University of Illinois at Urbana—Champaign, Urbana, Illinois 61801, United States*

**Toby J. Woods** − *Department of Chemistry, University of Illinois at Urbana—Champaign, Urbana, Illinois 61801, United States;* orcid.org/0000-0002-1737-811X

**Richard T. Haasch** − *Frederick Seitz Materials Research Laboratory, University of Illinois at Urbana—Champaign, Urbana, Illinois 61801, United States;* orcid.org/0000-0001-9479-2595

**Steven C. Zimmerman** − *Department of Chemistry, University of Illinois at Urbana—Champaign, Urbana, Illinois 61801, United States*

Complete contact information is available at: https://pubs.acs.org/10.1021/acscatal.4c01244


### Notes

The authors declare no competing financial interest.

## ■ ACKNOWLEDGMENTS

Q.H. acknowledges receipt of the J.C. Martin Memorial Student Travel Award and the LAS Department Award. The National Science Foundation (2029326) is gratefully acknowledged for supporting this research. J.C. and S.C.Z. acknowledge the National Science Foundation (CHE-1709718) for supporting this research.

## ■ REFERENCES


(1) Gewirth, A. A.; Varnell, J. A.; DiAscro, A. M. Nonprecious Metal Catalysts for Oxygen Reduction in Heterogeneous Aqueous Systems. *Chem. Rev.* **2018**, *118* (5), 2313−2339.

(2) Bai, J.; Yang, L.; Jin, Z.; Ge, J.; Xing, W. Advanced Pt-based intermetallic nanocrystals for the oxygen reduction reaction. *Chin. J. Catal.* **2022**, *43* (6), 1444−1458.

(3) Wu, D.; Shen, X.; Pan, Y.; Yao, L.; Peng, Z. Platinum Alloy Catalysts for Oxygen Reduction Reaction: Advances, Challenges and Perspectives. *ChemNanoMat* **2020**, *6* (1), 32−41.

(4) Xia, Z.; Zhu, R.; Yu, R.; Zhang, S.; Jung, J. C.-Y.; Zhang, J. Review—Recent Progress in Highly Efficient Oxygen Reduction Electrocatalysts: From Structural Engineering to Performance Optimization. *J. Electrochem. Soc.* **2022**, *169* (3), No. 034512.

(5) Wang, C.; Markovic, N. M.; Stamenkovic, V. R. Advanced Platinum Alloy Electrocatalysts for the Oxygen Reduction Reaction. *ACS Catal.* **2012**, *2* (5), 891−898.

(6) Ruban, A.; Hammer, B.; Stoltze, P.; Skriver, H. L.; Nørskov, J. K. Surface electronic structure and reactivity of transition and noble metals1Communication presented at the First Francqui Colloquium, Brussels, 19−20 February 1996.1. *J. Mol. Catal. A: Chem.* **1997**, *115* (3), 421−429.

(7) Hammer, B.; Nørskov, J. K. Electronic factors determining the reactivity of metal surfaces. *Surf. Sci.* **1995**, *343* (3), 211−220.

(8) Stamenkovic, V.; Mun, B. S.; Mayrhofer, K. J. J.; Ross, P. N.; Markovic, N. M.; Rossmeisl, J.; Greeley, J.; Nørskov, J. K. Changing the Activity of Electrocatalysts for Oxygen Reduction by Tuning the Surface Electronic Structure. *Angew. Chem.* **2006**, *118* (18), 2963−2967.

(9) Stamenkovic, V. R.; Fowler, B.; Mun, B. S.; Wang, G.; Ross, P. N.; Lucas, C. A.; Marković, N. M. Improved Oxygen Reduction Activity on Pt3Ni(111) via Increased Surface Site Availability. *Science* **2007**, *315* (5811), 493−497.

(10) Ando, F.; Gunji, T.; Tanabe, T.; Fukano, I.; Abruña, H. D.; Wu, J.; Ohsaka, T.; Matsumoto, F. Enhancement of the Oxygen Reduction Reaction Activity of Pt by Tuning Its d-Band Center via Transition Metal Oxide Support Interactions. *ACS Catal.* **2021**, *11* (15), 9317−9332.

(11) Kitchin, J. R.; Norskov, J. K.; Barteau, M. A.; Chen, J. G. Role of strain and ligand effects in the modification of the electronic and chemical properties of bimetallic surfaces. *Phys. Rev. Lett.* **2004**, *93* (15), No. 156801.

(12) Bligaard, T.; Nørskov, J. K. Ligand effects in heterogeneous catalysis and electrochemistry. *Electrochim. Acta* **2007**, *52* (18), 5512−5516.

(13) Schnur, S.; Groß, A. Strain and coordination effects in the adsorption properties of early transition metals: A density-functional theory study. *Phys. Rev. B* **2010**, *81* (3), No. 033402.

(14) Xia, Z.; Guo, S. Strain engineering of metal-based nanomaterials for energy electrocatalysis. *Chem. Soc. Rev.* **2019**, *48* (12), 3265−3278.

(15) Stamenkovic, V. R.; Mun, B. S.; Mayrhofer, K. J. J.; Ross, P. N.; Markovic, N. M. Effect of Surface Composition on Electronic Structure, Stability, and Electrocatalytic Properties of Pt-Transition Metal Alloys: Pt-Skin versus Pt-Skeleton Surfaces. *J. Am. Chem. Soc.* **2006**, *128* (27), 8813−8819.

(16) Marković, N. M.; Schmidt, T. J.; Stamenković, V.; Ross, P. N. Oxygen Reduction Reaction on Pt and Pt Bimetallic Surfaces: A Selective Review. *Fuel Cells* **2001**, *1* (2), 105−116.

(17) Strasser, P.; Koh, S.; Anniyev, T.; Greeley, J.; More, K.; Yu, C.; Liu, Z.; Kaya, S.; Nordlund, D.; Ogasawara, H.; Toney, M. F.; Nilsson, A. Lattice-strain control of the activity in dealloyed core−shell fuel cell catalysts. *Nat. Chem.* **2010**, *2* (6), 454−460.

(18) Li, M.; Zhao, Z.; Cheng, T.; Fortunelli, A.; Chen, C.-Y.; Yu, R.; Zhang, Q.; Gu, L.; Merinov, B. V.; Lin, Z.; Zhu, E.; Yu, T.; Jia, Q.; Guo, J.; Zhang, L.; Goddard, W. A.; Huang, Y.; Duan, X. Ultrafine jagged platinum nanowires enable ultrahigh mass activity for the oxygen reduction reaction. *Science* **2016**, *354* (6318), 1414−1419.

(19) Chattot, R.; Le Bacq, O.; Beermann, V.; Kuhl, S.; Herranz, J.; Henning, S.; Kuhn, L.; Asset, T.; Guetaz, L.; Renou, G.; Drnec, J.; Bordet, P.; Pasturel, A.; Eychmuller, A.; Schmidt, T. J.; Strasser, P.; Dubau, L.; Maillard, F. Surface distortion as a unifying concept and descriptor in oxygen reduction reaction electrocatalysis. *Nat. Mater.* **2018**, *17* (9), 827−833.
(20) Kim, J.-H.; Chang, S.; Kim, Y.-T. Compressive strain as the main origin of enhanced oxygen reduction reaction activity for Pt electrocatalysts on chromium-doped titania support. *Appl. Catal., B* **2014**, *158*−*159*, 112−118.
(21) Luo, M.; Sun, Y.; Zhang, X.; Qin, Y.; Li, M.; Li, Y.; Li, C.; Yang, Y.; Wang, L.; Gao, P.; Lu, G.; Guo, S. Stable High-Index Faceted Pt Skin on Zigzag-Like PtFe Nanowires Enhances Oxygen Reduction Catalysis. *Adv. Mater.* **2018**, *30* (10), No. 1705515.
(22) Luo, M.; Zhao, Z.; Zhang, Y.; Sun, Y.; Xing, Y.; Lv, F.; Yang, Y.; Zhang, X.; Hwang, S.; Qin, Y.; Ma, J.-Y.; Lin, F.; Su, D.; Lu, G.; Guo, S. PdMo bimetallene for oxygen reduction catalysis. *Nature* **2019**, *574* (7776), 81−85.
(23) Bu, L.; Zhang, N.; Guo, S.; Zhang, X.; Li, J.; Yao, J.; Wu, T.; Lu, G.; Ma, J.-Y.; Su, D.; Huang, X. Biaxially strained PtPb/Pt core/shell nanoplate boosts oxygen reduction catalysis. *Science* **2016**, *354* (6318), 1410−1414.
(24) Wang, L.; Zeng, Z.; Gao, W.; Maxson, T.; Raciti, D.; Giroux, M.; Pan, X.; Wang, C.; Greeley, J. Tunable intrinsic strain in two-dimensional transition metal electrocatalysts. *Science* **2019**, *363* (6429), 870−874.
(25) Chattot, R.; Asset, T.; Bordet, P.; Drnec, J.; Dubau, L.; Maillard, F. Beyond Strain and Ligand Effects: Microstrain-Induced Enhancement of the Oxygen Reduction Reaction Kinetics on Various PtNi/C Nanostructures. *ACS Catal.* **2017**, *7* (1), 398−408.
(26) Chen, C.; Kang, Y.; Huo, Z.; Zhu, Z.; Huang, W.; Xin, H. L.; Snyder, J. D.; Li, D.; Herron, J. A.; Mavrikakis, M.; Chi, M.; More, K. L.; Li, Y.; Markovic, N. M.; Somorjai, G. A.; Yang, P.; Stamenkovic, V. R. Highly Crystalline Multimetallic Nanoframes with Three-Dimensional Electrocatalytic Surfaces. *Science* **2014**, *343* (6177), 1339−1343.
(27) Niu, Z.; Becknell, N.; Yu, Y.; Kim, D.; Chen, C.; Kornienko, N.; Somorjai, G. A.; Yang, P. Anisotropic phase segregation and migration of Pt in nanocrystals en route to nanoframe catalysts. *Nat. Mater.* **2016**, *15* (11), 1188−1194.
(28) Liang, J.; Ma, F.; Hwang, S.; Wang, X.; Sokolowski, J.; Li, Q.; Wu, G.; Su, D. Atomic Arrangement Engineering of Metallic Nanocrystals for Energy-Conversion Electrocatalysis. *Joule* **2019**, *3* (4), 956−991.
(29) Kühl, S.; Gocyla, M.; Heyen, H.; Selve, S.; Heggen, M.; Dunin-Borkowski, R. E.; Strasser, P. Concave curvature facets benefit oxygen electroreduction catalysis on octahedral shaped PtNi nanocatalysts. *J. Mater. Chem. A* **2019**, *7* (3), 1149−1159.
(30) Chattot, R.; Martens, I.; Scohy, M.; Herranz, J.; Drnec, J.; Maillard, F.; Dubau, L. Disclosing Pt-Bimetallic Alloy Nanoparticle Surface Lattice Distortion with Electrochemical Probes. *ACS Energy Lett.* **2020**, *5* (1), 162−169.
(31) Sawant, K. J.; Zeng, Z.; Greeley, J. P. Origin of Stability and Activity Enhancements in Pt-based Oxygen Reduction Reaction Catalysts via Defect-Mediated Dopant Adsorption. *Angew. Chem., Int. Ed.* **2024**, *63* (5), No. e202312747.
(32) Hoshi, N.; Nakamura, M. Enhancement of the Activity for the Oxygen Reduction Reaction on Well-defined Single Crystal Electrodes of Pt by Hydrophobic Species. *Chem. Lett.* **2021**, *50* (1), 72−79.
(33) Kuzume, A.; Herrero, E.; Feliu, J. M. Oxygen reduction on stepped platinum surfaces in acidic media. *J. Electroanal. Chem.* **2007**, *599* (2), 333−343.
(34) Gómez-Marín, A. M.; Feliu, J. M. Oxygen reduction on nanostructured platinum surfaces in acidic media: Promoting effect of surface steps and ideal response of Pt(111). *Catal. Today* **2015**, *244*, 172−176.
(35) Kajiwara, R.; Asaumi, Y.; Nakamura, M.; Hoshi, N. Active sites for the hydrogen oxidation and the hydrogen evolution reactions on the high index planes of Pt. *J. Electroanal. Chem.* **2011**, *657* (1−2), 61−65.
(36) Bandarenka, A. S.; Hansen, H. A.; Rossmeisl, J.; Stephens, I. E. Elucidating the activity of stepped Pt single crystals for oxygen reduction. *Phys. Chem. Chem. Phys.* **2014**, *16* (27), 13625−13629.
(37) Liu, G.; Shih, A. J.; Deng, H.; Ojha, K.; Chen, X.; Luo, M.; McCrum, I. T.; Koper, M. T. M.; Greeley, J.; Zeng, Z. Site-specific reactivity of stepped Pt surfaces driven by stress release. *Nature* **2024**, *626* (8001), 1005−1010.
(38) Kale, M. B.; Borse, R. A.; Gomaa Abdelkader Mohamed, A.; Wang, Y. Electrocatalysts by Electrodeposition: Recent Advances, Synthesis Methods, and Applications in Energy Conversion. *Adv. Funct. Mater.* **2021**, *31* (25), No. 2101313.
(39) Hoang, T. T. H.; Verma, S.; Ma, S.; Fister, T. T.; Timoshenko, J.; Frenkel, A. I.; Kenis, P. J. A.; Gewirth, A. A. Nanoporous Copper-Silver Alloys by Additive-Controlled Electrodeposition for the Selective Electroreduction of CO(2) to Ethylene and Ethanol. *J. Am. Chem. Soc.* **2018**, *140* (17), 5791−5797.
(40) Liu, C.; Li, Z.; Yu, P.; Wong, H.-W.; Gu, Z. Vertically Aligned and Surface Roughed Pt Nanostructured Wire Array as High Performance Electrocatalysts for Methanol Oxidation. *ACS Appl. Energy Mater.* **2018**, *1* (8), 3973−3983.
(41) Shin, H. C.; Dong, J.; Liu, M. Nanoporous structures prepared by an electrochemical deposition process. *Adv. Mater.* **2003**, *15* (19), 1610−1614.
(42) Hoang, T. T. H.; Gewirth, A. A. High Activity Oxygen Evolution Reaction Catalysts from Additive-Controlled Electrodeposited Ni and NiFe Films. *ACS Catal.* **2016**, *6* (2), 1159−1164.
(43) Chen, X.; Chen, J.; Alghoraibi, N. M.; Henckel, D. A.; Zhang, R.; Nwabara, U. O.; Madsen, K. E.; Kenis, P. J. A.; Zimmerman, S. C.; Gewirth, A. A. Electrochemical CO2-to-ethylene conversion on polyamine-incorporated Cu electrodes. *Nat. Catal.* **2021**, *4* (1), 20−27.
(44) Hua, Q.; Alghoraibi, N. M.; Chen, X.; Gewirth, A. A. Enhanced Methanol Oxidation Using Polymer-Incorporated Rough Pt Electrodes. *ACS Catal.* **2023**, *13*, 10683−10693.
(45) Dhanasekaran, P.; Lokesh, K.; Ojha, P. K.; Sahu, A. K.; Bhat, S. D.; Kalpana, D. Electrochemical deposition of three-dimensional platinum nanoflowers for high-performance polymer electrolyte fuel cells. *J. Colloid Interface Sci.* **2020**, *572*, 198−206.
(46) Sandbeck, J. S.; On, D. Dissolution of Platinum: From Fundamental to Advanced Catalytic Materials, PhD Thesis; University of Erlangen−Nuremberg2020.
(47) Toyoda, E.; Jinnouchi, R.; Hatanaka, T.; Morimoto, Y.; Mitsuhara, K.; Visikovskiy, A.; Kido, Y. The d-Band Structure of Pt Nanoclusters Correlated with the Catalytic Activity for an Oxygen Reduction Reaction. *J. Phys. Chem. C* **2011**, *115* (43), 21236−21240.
(48) Hofmann, T.; Yu, T. H.; Folse, M.; Weinhardt, L.; Bär, M.; Zhang, Y.; Merinov, B. V.; Myers, D. J.; Goddard, W. A.; Heske, C. Using Photoelectron Spectroscopy and Quantum Mechanics to Determine d-Band Energies of Metals for Catalytic Applications. *J. Phys. Chem. C* **2012**, *116* (45), 24016−24026.
(49) Chen, K.; Liu, K.; An, P.; Li, H.; Lin, Y.; Hu, J.; Jia, C.; Fu, J.; Li, H.; Liu, H.; Lin, Z.; Li, W.; Li, J.; Lu, Y.-R.; Chan, T.-S.; Zhang, N.; Liu, M. Iron phthalocyanine with coordination induced electronic localization to boost oxygen reduction reaction. *Nat. Commun.* **2020**, *11* (1), No. 4173.
(50) Luo, M.; Zhao, Z.; Zhang, Y.; Sun, Y.; Xing, Y.; Lv, F.; Yang, Y.; Zhang, X.; Hwang, S.; Qin, Y.; Ma, J.-Y.; Lin, F.; Su, D.; Lu, G.; Guo, S. PdMo bimetallene for oxygen reduction catalysis. *Nature* **2019**, *574*, 81−85.
(51) Shinagawa, T.; Garcia-Esparza, A. T.; Takanabe, K. Insight on Tafel slopes from a microkinetic analysis of aqueous electrocatalysis for energy conversion. *Sci. Rep.* **2015**, *5*, No. 13801.
(52) Zhou, R.; Zheng, Y.; Jaroniec, M.; Qiao, S.-Z. Determination of the Electron Transfer Number for the Oxygen Reduction Reaction: From Theory to Experiment. *ACS Catal.* **2016**, *6* (7), 4720−4728.


https://doi.org/10.1021/acscatal.4c01244
*ACS Catal.* 2024, 14, 7526−7535

(53) Clavilier, J.; El Achi, K.; Rodes, A. In situ probing of step and terrace sites on Pt(S)-[n(111) × (111)] electrodes. *Chem. Phys.* **1990**, *141* (1), 1−14.
(54) Motoo, S.; Furuya, N. Effect of terraces and steps in the electrocatalysis for formic acid oxidation on platinum. *Ber. Bunsenges. Phys. Chem.* **1987**, *91* (4), 457−461.
(55) Santos, V. P.; Camara, G. A. Platinum single crystal electrodes: Prediction of the surface structures of low and high Miller indexes faces. *Res. Surf. Interfaces* **2021**, *3*, No. 100006.
(56) Diaz-Morales, O.; Hersbach, T. J. P.; Badan, C.; Garcia, A. C.; Koper, M. T. M. Hydrogen adsorption on nano-structured platinum electrodes. *Faraday Discuss.* **2018**, *210* (0), 301−315.
(57) Shah, A. H.; Wan, C.; Huang, Y.; Duan, X. Toward Molecular Level Understandings of Hydrogen Evolution Reaction on Platinum Surface. *J. Phys. Chem. C* **2023**, *127* (27), 12841−12848.
(58) Angerstein-Kozlowska, H.; Conway, B. E.; Sharp, W. B. The real condition of electrochemically oxidized platinum surfaces: Part I. Resolution of component processes. *J. Electroanal. Chem. Interfacial Electrochem.* **1973**, *43* (1), 9−36.
(59) Conway, B. E.; Jerkiewicz, G. Surface orientation dependence of oxide film growth at platinum single crystals. *J. Electroanal. Chem.* **1992**, *339* (1), 123−146.
(60) Conway, B. E. Electrochemical oxide film formation at noble metals as a surface-chemical process. *Prog. Surf. Sci.* **1995**, *49* (4), 331−452.
(61) Gewirth, A. A.; Thorum, M. S. Electroreduction of dioxygen for fuel-cell applications: materials and challenges. *Inorg. Chem.* **2010**, *49* (8), 3557−3566.
(62) Chen, W.; Xiang, Q.; Peng, T.; Song, C.; Shang, W.; Deng, T.; Wu, J. Reconsidering the Benchmarking Evaluation of Catalytic Activity in Oxygen Reduction Reaction. *iScience* **2020**, *23* (10), No. 101532.
(63) Sepa, D. B.; Vojnovic, M. V.; Damjanovic, A. Reaction intermediates as a controlling factor in the kinetics and mechanism of oxygen reduction at platinum electrodes. *Electrochim. Acta* **1981**, *26* (6), 781−793.
(64) Pasti, I. A.; Gavrilov, N. M.; Mentus, S. V. Potentiodynamic Investigation of Oxygen Reduction Reaction on Polycrystalline Platinum Surface in Acidic Solutions: the Effect of the Polarization Rate on the Kinetic Parameters. *Int. J. Electrochem. Sci.* **2012**, *7* (11), 11076−11090.
(65) Marković, N.; Gasteiger, H. A.; Grgur, B. N.; Ross, P. N. Oxygen reduction reaction on Pt(111): effects of bromide. *J. Electroanal. Chem.* **1999**, *467* (1), 157−163.
(66) Ghoneim, M. M.; Clouser, S.; Yeager, E. Oxygen Reduction Kinetics in Deuterated Phosphoric Acid. *J. Electrochem. Soc.* **1985**, *132* (5), 1160.
(67) Tse, E. C. M.; Varnell, J. A.; Hoang, T. T. H.; Gewirth, A. A. Elucidating Proton Involvement in the Rate-Determining Step for Pt/Pd-Based and Non-Precious-Metal Oxygen Reduction Reaction Catalysts Using the Kinetic Isotope Effect. *J. Phys. Chem. Lett.* **2016**, *7* (18), 3542−3547.
(68) Li, M. F.; Liao, L. W.; Yuan, D. F.; Mei, D.; Chen, Y.-X. pH effect on oxygen reduction reaction at Pt(111) electrode. *Electrochim. Acta* **2013**, *110*, 780−789.
(69) Lee, Y.-W.; Ko, A. R.; Kim, D.-Y.; Han, S.-B.; Park, K.-W. Octahedral Pt-Pd alloy catalysts with enhanced oxygen reduction activity and stability in proton exchange membrane fuel cells. *RSC Adv.* **2012**, *2* (3), 1119−1125.
(70) Wu, Y.; Zhao, Y.; Liu, J.; Wang, F. Adding refractory 5d transition metal W into PtCo system: An advanced ternary alloy for efficient oxygen reduction reaction. *J. Mater. Chem. A* **2018**, *6*, 10700−10709.
(71) Shu, Q.; Zhang, J.; Hu, B.; Deng, X.; Yuan, J.; Ran, R.; Zhou, W.; Shao, Z. Rational Design of a High-Durability Pt-Based ORR Catalyst Supported on Mn/N Codoped Carbon Sheets for PEMFCs. *Energy Fuels* **2022**, *36* (3), 1707−1715.
(72) Liu, X.-J.; Yin, X.; Sun, Y.-D.; Yu, F.-J.; Gao, X.-W.; Fu, L.-J.; Wu, Y.-P.; Chen, Y.-H. Interlaced Pd−Ag nanowires rich in grain boundary defects for boosting oxygen reduction electrocatalysis. *Nanoscale* **2020**, *12* (9), 5368−5373.
(73) Winand, R. Electrodeposition of metals and alloys—new results and perspectives. *Electrochim. Acta* **1994**, *39* (8), 1091−1105.
(74) Vela, M. E.; Marchiano, S. L.; Salvarezza, R. C.; Arvia, A. J. Growth of columnar gold electrodes by electroreducing hydrous gold oxide layers: kinetics and mechanistic interpretation. *J. Electroanal. Chem.* **1995**, *388* (1), 133−141.
(75) Jha, M. K.; Gupta, D.; Lee, J.-c.; Kumar, V.; Jeong, J. Solvent extraction of platinum using amine based extractants in different solutions: A review. *Hydrometallurgy* **2014**, *142*, 60−69.
(76) Ge, T.; Zhou, X.; Xu, L.; Sun, Y.; Yang, C.; Tian, Y.; Zhao, Z. Efficient extraction of platinum(IV) using tertiary-amine groups functionalized thiacalix[4]arene as extractant. *Miner. Eng.* **2024**, *206*, No. 108504.
(77) Mun, B. S.; Watanabe, M.; Rossi, M.; Stamenkovic, V.; Markovic, N. M.; Ross, P. N., Jr. A study of electronic structures of Pt3M (M = Ti,V,Cr,Fe,Co,Ni) polycrystalline alloys with valence-band photoemission spectroscopy. *J. Chem. Phys.* **2005**, *123* (20), No. 204717.
(78) Toyoda, E.; Hatanaka, T.; Takahashi, N.; Jinnouchi, R.; Morimoto, Y. Analysis of Electronic State of Pt Small Particles on Carbon Substrate by sXPS. *ECS Trans.* **2009**, *25* (1), 1057.
(79) Fortunelli, A.; Goddard, W. A., III; Sementa, L.; Barcaro, G.; Negreiros, F. R.; Jaramillo-Botero, A. The atomistic origin of the extraordinary oxygen reduction activity of Pt(3)Ni(7) fuel cell catalysts. *Chem. Sci.* **2015**, *6* (7), 3915−3925.
(80) Perrin, D. D. *Dissociation Constants of Organic Bases in Aqueous Solution: Supplement*; Pergamon, 1972.
(81) Swain, B.; Jeong, J.; Kim, S. K.; Lee, J. C. Separation of platinum and palladium from chloride solution by solvent extraction using Alamine 300. *Hydrometallurgy* **2010**, *104* (1), 1−7.


https://doi.org/10.1021/acscatal.4c01244
*ACS Catal.* 2024, 14, 7526−7535